Free surface flow over square bars at different Reynolds numbers

Razieh Jalalabadi[a,*], Thorsten Stoesser[a], Pablo Ouro[b], Qianyu Luo[a], Zhihua Xie[b]

[a]*Department of Civil, Environmental and Geomatic Engineering, University College London, Gower street, London, WC1E 6BT, UK*
[b]*Hydro-environmental Research Centre, School of Engineering, Cardiff University, The Parade, Cardiff, CF243AA, UK*

Abstract

Large-eddy simulations of free surface flow over bed-mounted square bars are performed for laminar, transitional and turbulent flows at constant Froude number. Two different bar spacings are selected corresponding to transitional and k-type (reattaching flow) roughness, respectively. The turbulent flow simulations are validated with experimental data and convincing agreement between simulation and measurement is obtained in terms of water surface elevations and streamwise velocity profiles. The water surface deforms in response to the underlying bed roughness ranging from mild undulation for transitional roughness to distinct standing waves for k-type roughness. The instantaneous water surface deformations increase with an increase in Reynolds number. Contours of the mean streamwise and wall-normal velocities, the total shear stress and the streamfunction reveal the presence and extension of recirculation zones in the trough between two consecutive bars. The flow is governed by strong local velocity gradients as a result of the rough bed and the deformed water surface. The local Froude number at the free surface increases for low Reynolds number in the flow over transitional roughness and decreases for low Reynolds number in the flow over k-type roughness. The transitional and turbulent flows exhibit a very similar distribution of the pressure coefficient C_p in both cases, whilst C_p

*Corresponding author
Email address: `r.jalalabadi@ucl.ac.uk` (Razieh Jalalabadi)

is generally lower for the laminar flow. Regarding the friction coefficient, C_f, it is significantly lower in the turbulent case than in the transitional and laminar cases. The bar spacing does not affect significantly the relative contribution of friction and pressure forces to the total force, neither does the Reynolds number. The friction factor is greater for transitional roughness and decreases with increasing Reynolds number.

Keywords: Free surface flow, large-eddy simulation, rough-bed flow, turbulent flow, transitional flow, laminar flow.

1. Introduction

Shallow flows over rough beds are ubiquitous in nature, in particular in relatively steep channels or when traveling at high Froude numbers. These flows are characterised by significant deformation of the water surface, localised standing waves or even hydraulic jumps. The nature of deformation of the water surface of shallow flows over rough beds is influenced by several parameters including the Froude and Reynolds number, the channel bed slope as well as the bed's roughness topography. The cause of water surface deformations is the bulk flow and its turbulence structure. Scrutinizing the water surface deformation as a result of bulk flow characteristics and turbulence structures in response to the channel's rough bed can lead to a detailed understanding of shallow free surface flow hydrodynamics and hence to advanced non-intrusive river gauging methods or aerial flow measurements.

The geometrical characteristics of the bed roughness manipulates the flow's quantities and their distributions such as the velocity profile and the total drag. Here, a train of two-dimensional square bars, placed on a bed perpendicular to the flow at a given bar spacing, comprises the roughness. The main two types of this roughness, known as d-type (closely spaced bars) and k-type (widely spaced bars), were first identified by Perry et al. (1969). They summarised that the effective roughness, which is used to characterise the drag increment due to the roughness (Jiminez, 2004), is proportional to the integral length scale of the flow for the d-type roughness and to the roughness height for the k-type roughness. Thus, at a given bulk Reynolds number, the transition between d- and k-type roughness over two-dimensional roughness elements depends only on the streamwise spacing of the bars. The mean and turbulent flow characteristics over square bar roughness have been investigated both experimentally (Okamoto, Seo, Nakaso and Kawai, 1993; Djenidi, Elavarasan and Antonia, 1999; Krogstad, Andersson, Bakken and Ashrafian, 2005; Djenidi, Antonia, Amielh and Anselmet, 2008; Roussinova and Balachandar, 1969) and numerically (Cui, Patel and Lin, 2003; Stoesser and Rodi, 2004; Ikeda and Durbin, 2007; Stoesser and Nikora, 2008; McSherry, Chua and Stoesser, 2017). Although this roughness geometry is rather simple, it has been helpful in studying the flow features over rough surfaces such as the transition from d- to k-type roughness which occurs at around $\lambda/k = 4 - 5$, where λ is the crest-to-crest bar spacing and k is the bar height (Simpson, 1973; Tani, 1987; Jiminez, 2004). Although many of the works mentioned focused on single-phase flows (closed channels), some investigated free surface flows over bars where the submergence plays a key role in the formation of the flow structure. In flows with large submergence, the entire cavity between roughness elements is occupied by a stable vortex for d-type roughness; however, for k-type roughness the flow reattaches to the bed after a wake region between two bars (Stoesser and Rodi, 2004). Stoesser and Nikora (2008) used large-eddy simulation (LES) for free surface flow with intermediate submergence and showed that for $\lambda/k > 8$ the bars are isolated and the flow reattaches to the bed between two square bars. This was also shown in single-phase flows (Leonardi, Orlandi, Smalley, Djenidi and Antonia, 2003). Experiments of the flow with different submergence for two k-type spacings (λ/k = 9 and 18) revealed that for the larger spacing the roughness effect extends up to a distance of $3k$ from the bed while for smaller spacing the outer layer is affected by the roughness too. In flows with low submergence, the free surface experience changes due to the roughness especially in the form of standing wave or hydraulic jump at the free surface. These surface modulations are mainly generated over k-type roughness. Large scale turbulent structures, strong turbulence production and energy dissipation contribute to these deformation at the free surface (Chanson and Brattberg, 2000; Chanson, 2009). McSherry et al. (2018) carried out several LES and laboratory experiments to study the hydrodynamics of shallow flows and quantified the effects of roughness spacing and relative submergence on hydraulic resistance in such flows. Six flow cases, with transitional (between d- and k-type) and k-type roughness types and varying relative submergence were investigated. Flow features such as free surface deformation, double averaged velocities and shear stresses and the contributions to the overall momentum balance were presented.

The research reported here investigates shallow flows over a transitional and a k-type roughness at three Reynolds numbers resulting in laminar, transitional and turbulent flow at the same Froude number. The objective of the present work is to investigate the effect of Reynolds number on the free surface characteristics, the underlying hydrodynamics, the distribution of the fluid stress and the relative contributions of pressure and friction drag to the total drag of shallow flows over bar-roughened beds. This paper is organized in four sections. Section 2 describes the applied numerical method and details of the simulations, section 3 presents and discusses the results. The manuscript is wrapped up by a summary and conclusion in section 4.

2. Numerical framework and simulations performed

Large-eddy simulation (LES) is employed in this research, a method perceived to be particularly suitable to simulate flows which are affected by large-scale turbulence structures (Stoesser, 2014). Due to the eddy-resolving nature of this approach energetic large-scale structures of the flow are calculated directly and the effect of the small scales on the large scales is modelled. Another time-resolved computational method, unsteady Reynolds-averaged Navier-Stokes (URANS), is deemed unsuitable for this due its inability to predict accurately and reliably flow separation and reattachment, an important feature of the flows under consideration. Direct numerical simulation (DNS) is the only approach which resolves all scales of turbulence but it is computationally uneconomical and requires enormous computational resources. The in-house LES code HYDRO3D is employed to simulate the flows reported in this study. It has been validated thoroughly for a large number of flows of similar complexity (Stoesser, 2010; Bomminayuni and Stoesser, 2011; Stoesser, McSherry and Fraga, 2015; Fraga, Stoesser, Lai and Socolofsky, 2016b; Fraga and Stoesser, 2016a; Ouro, Harrold, Stoesser and Bromley, 2017a; Ouro and Stoesser, 2017b).The code solves the spatially filtered Navier-Stokes equations

$$\nabla \cdot \mathbf{u} = 0 \tag{1}$$

$$\frac{\partial \mathbf{u}}{\partial t} + \mathbf{u} \cdot \nabla \mathbf{u} = -\nabla p + \frac{1}{Re} \nabla^2 \mathbf{u} - \nabla \cdot \tau \tag{2}$$

for turbulent, incompressible, three-dimensional flow. In equations (1) and (2) $\mathbf{u}$ is the velocity vector with the three components u, v, w in the streamwise (x), spanwise (y) and wall-normal (z) directions, p is the pressure, τ is the subgrid scale stress tensor, $Re = U_b H/\nu$ is the Reynolds number where U_b is the bulk velocity, H is the depth defined as the distance between the mean water surface position before starting the simulation and the mean bed elevation (see Fig. 1), and ν is the fluid kinematic viscosity. The effects of the small-scale turbulence on the large eddies is approximated using the Wall-Adapting Local Eddy-viscosity (WALE) (Nicoud and Ducros, 1999) model. There are several advantages of using this model compared to the classical Smagorinsky model such as detecting all the turbulent structures relevant to kinetic energy dissipation and/or no need of a damping function or constant adjustments near the wall as the eddy-viscosity goes naturally to zero in that region. A fractional-step method with a second order Runge-Kutta time integration scheme is used to solve equations (1) and (2) on a staggered Cartesian grid. In the predictor step a second order finite difference method is used to compute diffusive terms and a fifth-order weighted, essentially non-oscillatory (WENO) scheme is used to compute the convective terms (Shu, 2009). The WENO scheme offers the necessary compromise between numerical accuracy and algorithm stability which is especially important for the free-surface algorithm (Kara, Kara, Stoesser and Sturm, 2015b). A multi-grid method is employed in the corrector step to solve the pressure Poisson equation and to achieve a divergent flow field at the end of each time step. The accuracy and credibility of LES results are more sensitive to the treatment of boundary conditions, also called super-grid modeling, and use of high-order spatial discretization schemes together with sufficiently fine grids (Stoesser, 2014; Rodi, Constantinescu and Stoesser, 2013). Validating the present results with similar experiments (Fig. 2) shows that the numerical implementation of the Navier-Stokes equations are accurate enough for the applied grid resolution. The Level Set Method (LSM), proven to be successful in the description of complex air–water interfaces, is used for free surface capturing(Sussman, Smereka and Osher, 1994; Kang and Sotiropoulos, 2012; Kara, Stoesser, Sturm and Mulahasan, 2015c; Kara, Kara, Stoesser and Sturm, 2015b). A level set signed distance function, ϕ, which is zero at the phase interface, negative in air and positive in water is employed. The interface is tracked by solving a pure advection equation (Sethian and Smereka, 2003)

$$\frac{\partial \phi}{\partial t} + \mathbf{u} \cdot \nabla \phi = 0 \tag{3}$$

A transition zone is introduced at either side of the phase interface to avoid numerical instability. This instability may be caused due to sudden change and discontinuity of density and viscosity of the two immiscible fluids. In the transition zone, with the thickness of two grid spacings, ϕ is calculated as $|\phi| \leq \varepsilon$ where ε is half of the thickness of the interface. The density ρ and dynamic viscosity μ are calculated as

$$\rho(\phi) = \rho_g + (\rho_l - \rho_g)\mathcal{H}(\phi) \tag{4}$$

$$\mu(\phi) = \mu_g + (\mu_l - \mu_g)\mathcal{H}(\phi) \tag{5}$$

where $\mathcal{H}(\phi)$ is a Heaviside defined as $\mathcal{H}(\phi) = 0$ for $\phi < -\varepsilon$, $\mathcal{H}(\phi) = 1/2(1 + \phi/\varepsilon + \sin(\pi\phi/\varepsilon)/\pi)$ for $|\phi| < \varepsilon$ and $\mathcal{H}(\phi) = 1$ for $\phi > \varepsilon$. Equation (3) is solved using the WENO scheme as this is a pure advection problem and using central differencing schemes cause stability problem(Rodi, Constantinescu and Stoesser, 2013). The solution domain is decomposed into a certain number of sub-domains and the code solves the equations in each domain separately via parallel computing. The Message Passing Interface (MPI) is used to allow communication between sub-domains. More details of the code can be found in (Cevheri, McSherry and Stoesser, 2016; Ouro, Fraga, Lopez-Novoa and Stoesser, 2018; Kara, Stoesser and McSherry, 2015a)

Large-eddy simulations of the flow over two-dimensional square bars of height (k) at two different bar spacings, $\lambda/k = 5.2$ and $\lambda/k = 10.4$, where λ is the distance from bar to bar, are carried out at three different Re, corresponding to laminar, transitional and turbulent flow are performed. Table 1 provides an overview of the various simulations as well as geometrical and hydraulic parameters for each case. The $\lambda/k = 5.2$ case is neither d-type (skimming flow) nor k-type (reattaching flow) roughness so it is considered transitional (wake interference flow) roughness, while the $\lambda/k = 10.4$ case is classified as k-type roughness. The global Froude number, $Fr = U_b/\sqrt{gH}$, is kept constant for all cases (g is the gravity acceleration). The two turbulent flows are carried out at two different grid resolutions (medium and fine) and also double-sized domain (double the length and width in streamwise and spanwise directions, respectively) to investigate the sensitivity of the simulation results to grid resolution and domain size. Fig. 1 presents the schematic of the computational domains. For both bars spacings the length of the domain, L_x, is $10.4k$, the width, L_y , and height (including both water and air), L_z, are both $5k$ and hence for the $\lambda/k = 5.2$ case the domain included two troughs while for $\lambda/k = 10.4$ it only contained one trough. For the double-sized domain the streamwise and the spanwise extent of the domain are doubled without changing the grid resolution and for the fine grid the grid numbers are doubled in all directions on the regular-sized domain. In all cases the grid spacing is uniform in all directions. The geometrical configurations and flow variables are generally similar to the experiments and simulations of McSherry et al. (2018) while some details regarding boundary conditions and flow simulations differs. A no-slip boundary condition is applied at the bottom and at the surface of the bars. Periodic boundary condition are applied in the streamwise and spanwise directions to ensure that the flow is quasi two-dimensional (i.e. homogeneous in the spanwise direction) and without secondary currents (McSherry et al., 2018). The turbulent and transitional flows simulations are driven by a constant pressure gradient of similar value to the flume experiments discussed in McSherry et al. (2018) while the laminar simulations are driven by an adjusted pressure gradient to maintain a constant mass flow rate to ensure that U_b is similar to the turbulent cases. The friction velocity, as listed in Table. 1, used to calculate the grid spacings in wall units, is calculated from $U_\tau = (dp/dx)(h/\rho)$ where dp/dx is the pressure gradient in the streamwise direction and h is the mean water surface elevation from the bed at still water level (see Fig. 1). All simulations are initiated with a free-slip boundary condition at the still water level and the simulations are run for 10 to 15 flow through periods, T_f $(= L_x/U_b)$, to allow for the flow to develop fully. The simulations are then restarted with the level set algorithm to track the free surface. Averaging of the flow quantities is begun after another 4 to 6 flow through periods when the free-surface flow is fully developed, and continued for between 40 and 60 further flow through periods to obtain converged turbulence statistics. The differences in Fr and Re between the work of McSherry et al. (2018) and the present simulations for turbulent flows is due to uncertainties in the experiments. However, the difference in Fr or Re is less than 10% or 5%, respectively for the turbulent flows suggesting adequacy of grid, domain size and boundary conditions. In this following, time-averaged quantities are denoted with an overbar, the double- (temporal- and spatial-) averaged quantities are denoted by both the overbar and brackets $< >$, the small symbols with prime are fluctuations and small symbols without any of these are instantaneous quantities.

3. Results and discussion

The credibility of the simulations is assessed first by comparing computed two-dimensional water surface elevation and the temporal mean streamwise velocity of the two turbulent cases with data reported in McSherry et al. (2018). Fig. 2 (a,b) present time- and spanwise-averaged water surface elevations for all grid spacings and domain sizes together with experimental and numerical data (case C2 and C5) in McSherry et al. (2018). There is a good agreement between the present LES results and the reference data. Fig. 2 (c,d) show the adequacy of the domain size and grid spacing chosen for the turbulent case as well. Fig. 3 and Fig. 4 show profiles of the time- and spanwise-averaged streamwise velocity together with the corresponding data reported in McSherry et al. (2018) from both experiments and LES. There were two measurement locations for $\lambda/k = 5.2$ and four for $\lambda/k = 10.4$ (Fig. 1). Both figures show good agreement of the present results with McSherry et al. (2018)'s data. The results of the simulations on the fine grid and with the double domain (not shown here) are similar to the results obtained on the chosen domain and grid size and are hence not worth presenting. The simulation outputs in terms of turbulence statistics are not sensitive to the grid resolution and domain size. The grid resolution of the transitional Re is identical to the grid resolution of the turbulent cases while the the laminar cases were carried out on a coarser grid, however due to the low Reynolds number the grid is effectively finer than for the other two cases. Table 1 demonstrates the adequacy of the grid size for all simulated cases.

3.1. Water surface

The time- and spanwise-averaged water surface profile is plotted in Fig. 5 for all Re simulated. There was no considerable difference in water surface between the three flow cases over the $\lambda/k = 5.2$ bars except for some weak undulation between two consecutive bars in the turbulent and transitional flows, whilst the free surface of the laminar flow is almost flat. Over the $\lambda/k = 10.4$ bars the general feature of the water surface is similar for all Re, exhibiting a standing wave between the bars. Increasing the Re results in the standing wave becoming steeper with the trough of the wave deeper. Fig. 6 shows the instantaneous three dimensional free surface of all six flows considered highlighting the differences in water surface behaviour of the simulated cases. The main difference for both $\lambda/k = 5.2$ and $\lambda/k = 10.4$ is that the water surface is the more disturbed the higher the Re. Instantaneous water surface disturbances are absent for the laminar cases and featured only a very weak undulation and a small standing wave for every two bars, Fig. 6(a) and (d) respectively. In the transitional Re, water surfaces are disturbed and the undulations over the $\lambda/k = 5.2$ bars and the standing wave over the $\lambda/k = 10.4$ bars are distinguished more clearly. In the turbulent flows, instantaneous water surface disturbances, the undulations and standing waves are well-established for both roughness arrangements. Due to the temporal- and spanwise-averaging instantaneous disturbances of the water surface are not seen in Fig. 5. The main features of the water surfaces are similar for all Re and for both $\lambda/k = 5.2$ and $\lambda/k = 10.4$, by increasing Re the instantaneous perturbations of the water surface are enhanced and modulate the time-averaged water surfaces.

3.2. Mean velocity contours and streamfunction

The velocity and stress distributions are examined to provide a more detailed understanding of the flow fields and momentum transport. Fig. 7 presents contours of the time- and spanwise-averaged streamwise velocity normalized by the bulk velocity for all six flow cases. Also plotted is the local Fr calculated at the free surface. In all cases the flow separates at the bars leading to the generation of recirculation bubbles just downstream of the bars. The recirculation zones include significant negative velocity near the bed in the transitional and turbulent flows over both bars spacing. In the flow over the $\lambda/k = 5.2$ bars this recirculation bubble occupied the entire trough between two consecutive bars while over $\lambda/k = 10.4$ this zone extends to a reattachment point after which the flow recovers to a boundary layer. The recirculation zone is the longest in the transitional flow and shortest in the laminar flow. The large shear stress in the laminar flow leads to boundary layer formation near the wall earlier than two other types of flow and this pushes the reattachement point back towards the bars which generates smaller recirculation zone. In turbulent flow, where there are the strongest disturbances, the intense mixing near the wall increase the momentum exchange. This affects the weak negative streamwise velocity at the end of the recirculation bubble hence contributes to a small recirculaton zone. In the transitional flow though, the shear stress and the turbulent motions are not at their maximum strength thus the negative streamwie velocity induced by the bar extends to a larger area and makes the recirculation zone the longest. In the flow over $\lambda/k = 5.2$ streamwise gradients of the streamwise velocity are almost absent above the bars while they are quite significant above the bars over $\lambda/k = 10.4$. The flow accelerates just above the bars near the free surface leading to a local increase of Fr until it reaches a maximum, after that the flow decelerates as the height of the recirculation bubble decreases relatively and the water depth increases suddenly hence a decrease in the streamwise velocity keeps a constant mass flow rate. This sudden deceleration is evidenced by the collapse in the local Fr. Local acceleration followed by a sudden deceleration results in the formation of the standing wave at the water surface (McSherry, Chua, Stoesser and Mulahasan, 2018). Fig. 7a, b, c show that the variations of the local Fr is significantly less in the $\lambda/k = 5.2$, and hence local variations of the water depth for these cases are much smaller, resulting in the aforementioned mild undulations. Noteworthy are high local Fr in the laminar case over the $\lambda/k = 5.2$ bars, which is due to the significant viscous stress, resulting in a quasi-parabolic velocity profile and consequently high streamwise velocities near the water surface.

The distribution of the total shear stress (viscous plus turbulent) signifies momentum flux. Contours of the the sum of the time- and spanwise-averaged shear stresses, viscous and Reynolds shear stress, normalized by the squared (global) shear velocity are shown in Fig. 8. In the laminar flow over $\lambda/k = 5.2$ the time-averaged shear stress is negative near the water surface, whereas in the transitional and turbulent flows it is near zero almost everywhere. The ever-soslightly deformed water surface in this case creates local form drag and hence the flow decelerates very close to the water surface. The negative shear stress is the result of negative streamwise velocity gradients and this is particularly pronounced in the laminar flow in which the viscosity is very high. In the laminar flow over $\lambda/k = 10.4$ the mean shear stress is negative just below the water surface as well and also in the transitional flow while it is positive upstream of the standing wave in the turbulent flow. The standing wave creates significant drag below the water surface, again leading to decelerated flow near the surface. In the laminar flow the extent of the negative shear stress is quite significant as there are large changes in the surface elevation especially around the standing wave. Due to high viscosity the effects of large water surface deformations in this case extend to larger flow depth hence the negative shear stress in this case is weaker than that in the laminar flow over $\lambda/k = 5.2$ as the boundary layer is thicker in the former than the latter. In the transitional flow the negative shear stress is only significant just downstream of the standing wave as the viscous effects are still considerable whereas in the turbulent flow it is strongest only immediately downstream of the wave as larger disturbances especially at the standing wave induce large disturbances in the flow field and contribute to larger turbulent shear stress. In the laminar flow in both geometries the maximum of the time- and space-averaged shear stress is at the crest of the bars where the velocity gradient is the largest but in the transitional and turbulent flows this maximum is downstream of the bars, due to only small contributions of the viscous stress and large contributions of the turbulent stress at higher *Re*. The effect of high viscosity is also observed near the bed. In the laminar flows pockets of the negative time- and space-averaged total shear stress are visible downstream of the bar (as a result of recirculation). In the transitional flows though, these pockets are visibly smaller, due to the viscous stress being less dominant and in the turbulent flows, where the viscous stress contribution is very small, they are reduced to a very thin layer adjacent to the wall in the recirculation bubbles.

Contours of the time- and spanwise-averaged wall-normal velocity normalized by the bulk velocity are presented in Fig. 9 and they highlight significant interaction of the near bed flow with the flow near the water surface, evidenced by pronounced variations of $<\overline{w}>$ over the water depth and in the streamwise direction. In the flows over $\lambda/k = 5.2$, alternating regions of positive and negative $<\overline{w}>$ are found above and below the crest of the bars. In the laminar flow, under the crest of the bars, there are mainly patches of positive $<\overline{w}>$ in the wake of the bars followed by negative $<\overline{w}>$. The positive patches occupy almost the entire cavity between bars in the transitional and turbulent flows and the regions of negative $<\overline{w}>$ are small but strong near the leading edge of the bars. Positive patches near the bed between the bars result in negative ones above extending up to the water surface. At the leading edge of the bars there is local increase in $<\overline{w}>$ resulting in regions of positive $<\overline{w}>$ above extending to the water surface. Alternating regions of positive and negative time- and spanwise-averaged wall-normal velocity are present in the flow over $\lambda/k = 10.4$ too. The patches of negative $<\overline{w}>$ above the crest of the bars results in regions of strong mean wall-normal velocity near the water surface and extending close to the bed between bars in the larger-spacing-simulations. Positive regions of $<\overline{w}>$ near the leading edge of the bars extend all the way to the water surface. A second peak of positive $<\overline{w}>$ is observed just below the standing wave. Clearly, maxima and minima of $<\overline{w}>$ are greater in the flow over the $\lambda/k = 10.4$ bars than over the $\lambda/k = 5.2$ bars. Fig. 7 and Fig. 9 suggest that the abrupt change of the water surface correlate with local acceleration/deceleration of the flow. These two figures also show that in the flow over $\lambda/k = 5.2$ under the crest of the bars there is flow circulation between two bars while in the flow over $\lambda/k = 10.4$ there is not such flow circulation.

Fig. 10 presents contour lines of the spanwise-mean streamfunction for all simulated cases. The dashed lines denote negative values. Consistent with Fig. 7 these plots show that for small bar spacing the recirculation zone occupies the cavity between bars while the mean flow reattaches at the bed for the wide bar spacing beds. Small regions of positive streamfunction, a secondary recirculation zone, driven by the primary recirculation, exists just downstream of the the bars and they are are of similar size in all transitional and turbulent cases. No such secondary recirculation zone exists in the laminar flow as a result of the primary recirculation being short and weak. There is a small region of negative streamfunction at the leading edge of the bars in the transitional and turbulent cases as the flow accelerates around the leading edge of the bars and detaching from the bed. The streamwise velocity near the bed in the laminar case is significantly smaller than in the other two flows and hence this upstream bubble is absent in the laminar flow. The longest recirculation bubble is found in the transitional flow due to the positive mean shear stress downstream of the bar as shown in Fig. 8. In the turbulent flow the streamwise extension of the recirculation zone is smaller due to the larger contribution of Reynolds shear stress to the mean shear stress which results in the larger region of positive mean shear stress downstream of the bar.

3.3. Pressure and friction forces

To investigate the interaction of the bulk flow with the bed, the main forces applied on the bed were studied. Pressure coefficient, C_p, which is the ratio of pressure difference over the dynamic pressure calculated by the bulk velocity and friction coefficient, C_f, which is the wall shear stress normalized by the dynamic pressure calculated by the bulk velocity were examined.

Fig. 11 plots $C_p = (< \overline{P} > - < \overline{P_{ref}} >) \; / \; (0.5\rho \, U^2{}_{\mathrm{b}})$ where $<\overline{P_{ref}}>$ is the temporal and spanwise mean pressure over the free surface at $x = x_{ref}$ (Fig. 1). In both roughness spacings, the pressure has its maximum value at the leading edge of the bars. In the transitional and turbulent flows there are no changes in C_p downstream of the bars up to some certain streamwise locations but it increased monotonously after this length with an abrupt sudden increase at the leading edge of the next bar. However, the increasing trend is found in the entire cavity for C_p in the laminar flows. In the flow over $\lambda/k = 5.2$ the length over which the pressure is constant is longer in the transitional and turbulent flows than that in those flows over $\lambda/k = 10.4$. C_p in the transitional and turbulent flows over both roughness types have similar values with the maximum C_p corresponding to the transitional flow. In the laminar flow, C_p is smaller while the difference of C_p between the laminar flow and two other flow cases is greater in the flow over $\lambda/k = 10.4$ than $\lambda/k = 5.2$. Since there is not a large difference between the mean relative submergence for all Re in both geometries (see Fig 5) and there is no dynamic pressure over the surface, C_p can be interpreted as the static pressure over the bed. In the flow over $\lambda/k = 5.2$ the values of the wall-normal velocity near the bed are smaller compared to the value and peaks of $<\overline{w}>$ in the flow over $\lambda/k = 10.4$ which are also closer to the bed (Fig. 9). This contributes to the generation of a larger pressure coefficient on the bed in the flow over $\lambda/k = 10.4$ as seen in Fig. 11.

Fig. 12 presents the friction coefficient $C_f = (\tau_{\mathrm{wall}})\ /\ (0.5\rho U^2{}_{\mathrm{b}})$ where τ_{wall} is the wall shear stress. The sign of C_f for all cases is consistent with the mean streamwise velocity distribution shown in Fig. 7. Here the friction coefficients in the two transitional flows are of the same order as those of the laminar flow cases. The negative peak of C_f in the transitional flow in Fig. 12(a) are further from the the trailing edge of the bar on the left compared to the same peak in the laminar flow due to the presence of the relatively larger region of the positive streamwise velocity in the wake of that bar (Fig. 7(a,b)). Having a smaller region of positive $<\overline{u}>$ in the turbulent flow in this case leads to the displacement of this peak back towards the upstream bar. Similarly, in Fig. 12(b) the first negative peak ($1.5 < x/k < 3$) is the furthest from the left bar in the transitional flow as the region of the positive streamwise velocity is the largest in this type of flow. The small recirculation region in $9 < x/k < 10$ in Fig. 7(d,f) leads to the generation of the second negative peak in Fig. 7(b) in the transitional and turbulent flows which causes a decrease in the total C_f in this geometry. Since the viscosity is larger in the laminar flow, the largest value of C_f is expected for both peaks in the laminar flow between the three simulated Re which is the case in Fig. 12 (b). But in the flow over $\lambda/k = 5.2$ the value of the negative peak is similar in the laminar and transitional flows representing the similar maximum tangential velocity above the bed between these two flow types.

The pressure and friction drag forces in the streamwise direction are shown in Fig. 13 a. These forces are normalized by the total force $F_T = F_\tau + F_P$. Friction drag is calculated at the bed and at the top of the bars and pressure drag is calculated at the front and back faces of the bars. Friction forces are entirely negative in flow over the $\lambda/k = 5.2$ bars (as the recirculation zone occupies the entire through), irrespective of Re, and just positive in all flows over the $\lambda/k = 10.4$ bars due to the recirculation zone being finite. In all cases, pressure drag is significantly larger than friction drag independent of the Reynolds number. Also, the bar spacing does not affect the distribution of the forces for the three Re investigated. Fig. 13 b plots friction factors (in the form of the Darcy Weisbach friction factor) as a function of Reynolds number for both roughness types. The friction factor of the flow over k-type roughness is consistently greater than for the flow over transitional roughness and this is in line with previous research. Also in line with previous research of flows over rough beds is that flow resistance decreases with an increase in Reynolds number.

4. Conclusions

Results of large-eddy simulations of flows over spanwise aligned square bars in an open channel flow were presented. Two bar spacings corresponding to transitional and k-type roughness were considered each at three Re corresponding to laminar, transitional and turbulent flows at a constant Fr. The time- and spanwise-averaged water surface profiles and the instantaneous three-dimensional water surface visualisations showed that the mean water surface deformations are similar for all three Re except for the effects of turbulence which results in perturbations of the instantaneous water surface. In the flow over k-type roughness a standing wave is established at all Re at the water surface and it is steepest in the turbulent flow. The flows over the transitional roughness are characterised by mild water surface undulations at all Re with these being most pronounced for the turbulent flow. Significant streamwise gradients of the time-averaged streamwise velocity, mainly occurring near the free surface and below the crest of the bars, are present in the flow over the k-type roughness. It was also revealed that the variations of the local Fr explained the formation of the standing waves, signifying a sudden drop in streamwise velocity near the water surface and hence a sudden deceleration of the flow leading to a sudden increase in water depth. The mean total shear stress is negative just below the water surface in the laminar flows over both bar spacing and its maximum value was in the flow over transitional roughness. This led to the rise of Fr to its largest value at the free surface in this flow type. The time-averaged wall-normal velocity varies significantly throughout the domain regardless of bar arrangement and Reynolds number. There is flow circulation below the crest of the bars over transitional roughness occupying the entire trough between bars. The largest recirculation bubble in the flow over k-type roughness was found in the transitional flow as the positive mean shear stress in the wake of the bars shifted the recirculation zone away from them. The larger contribution of Reynolds shear stress to the mean shear stress in the turbulent flow resulted in the decrease of the streamwise extension of the recirculation zone in this flow type. The maximum value of pressure on the bed corresponds to the transitional flows and the minimum value to the laminar flows in flow over both bar spacings. The peak of the pressure in every flow case occurs at the leading edge of the bars. Larger wall-normal velocity in the flow over k-type roughness contributes to larger C_p in this geometry. Small regions of positive streamwise velocity shifts the peak of C_f in the streamwsie direction. The tangential velocity adjacent to the wall is lager in the laminar flow over transitional roughness than k-type roughness, the cases in which the friction coefficients are maximum between all investigated Re. In the flow cases studied here, increasing the Re leads to a small increase in the pressure force applied on the bed and a small decrease in the viscous force while the bar spacing had even a smaller effect on the value of these forces. Generally pressure drag dominates this flow. In terms of friction factors, as expected k-type roughness features larger flow resistance and flow resistance generally decreases with an increase in Reynolds number.

Acknowledgements

Financial support was provided by the EPSRC/UK project "Rapid Monitoring of River Hydrodynamics and Morphology using Acoustic Holography", grant number EP/R022135/1. The fine-grid and large-domain large-eddy simulations were carried out on UCL's high performance computer Grace.

References

Bomminayuni, S., Stoesser, T., 2011. Turbulence statistics in an open-channel flow over a rough bed. J. Hydraul. Eng. 137(11), 1347–1358. doi:https://doi.org/10.1061/(ASCE)HY.1943-7900.0000454.

Cevheri, M., McSherry, R., Stoesser, T., 2016. A local mesh refinement approach for large-eddy simulations of turbulent flows. Int. J. Numer. Meth. Fluids. 82(5), 261–285. doi:https://doi.org/10.1002/fld.4217.

Chanson, H., 2009. Current knowledge in hydraulic jumps and related phenomena. a survey of experimental results. Eur. J. Mech. B Fluids. 28, 191–210. doi:10.1016/j.euromechflu.2008.06.004.

Chanson, H., Brattberg, T., 2000. Experimental study of the air-water shear flow in a hydraulic jump. Int. J. Multiph. Flow. 26(4), 583–607. doi:10.1016/S0301-9322(99)00016-6.

Cui, J., Patel, V.C., Lin, C.L., 2003. Large-eddy simulation of turbulent flow in a channel with rib roughness. Int. J. Heat Fluid Fl. 24, 372–388. doi:http://dx.doi.org/10.1016/S0142-727X(03)00002-X.

Djenidi, L., Antonia, R.A., Amielh, M., Anselmet, F., 2008. A turbulent boundary layer over a two-dimensional rough wall. Exp. Fluids. 44, 37–43. doi:https://doi.org/10.1007/s00348-007-0372-5.

Djenidi, L., Elavarasan, R., Antonia, R.A., 1999. The turbulent boundary layer over transverse square cavities. J. Fluid Mech. 395, 271–294. doi:https://doi.org/10.1017/S0022112099005911.

Fraga, B., Stoesser, T., 2016a. Influence of bubble size, diffuser width, and flow rate on the integral behaviour of bubble plumes. J. Geophys. Res. Solid Earth. 121(6), 3887–3904. doi:https://doi.org/10.1002/2015JC011381.

Fraga, B., Stoesser, T., Lai, C.C.K., Socolofsky, S.A., 2016b. A les-based eularian-lagrangian approach to predict the dynamics of bubble plumes. Ocean Model. 97, 27–36. doi:https://doi.org/10.1016/j.ocemod.2015.11.005.

Ikeda, T., Durbin, P., 2007. Direct numerical simulations of a rough-wall channel flow. J. Fluid Mech. 571, 235–263. doi:https://doi.org/10.1017/S002211200600334X.

Jiminez, J., 2004. Turbulent flows over rough walls. Annu. Rev. Fluid Mech. 36(4), 173–196. doi:https://doi.org/10.1146/annurev.fluid.36.050802.122103.

Kang, S., Sotiropoulos, F., 2012. Numerical modeling of 3d turbulent free surface flow in natural waterways. Adv. Water Resour. 40, 23–36. doi:https://doi.org/10.1016/j.advwatres.2012.01.012.

Kara, M., Stoesser, T., McSherry, R., 2015a. Calculation of fluid-structure interaction: methods, refinements, applications. Engineering and Computational Mechanics 168, 59–78. doi:https://doi.org/10.1680/eacm.15.00010.

Kara, S., Kara, M.C., Stoesser, T., Sturm, T.W., 2015b. Free-surface versus rigid-lid les computations for bridge-abutment flow. J. Hydraul. Eng. 141(9), 04015019. doi:doi:10.1061/(ASCE)HY.1943-7900.0001028.

Kara, S., Stoesser, T., Sturm, T., Mulahasan, S., 2015c. Flow dynamics through a submerged bridge opening with overtopping. J. Hydraul. Res. 53(2), 186–195. doi:10.1080/00221686.2014.967821.

Krogstad, P.A., Andersson, H.I., Bakken, O.M., Ashrafian, A., 2005. An experimental and numerical study of channel flow with rough walls. J. Fluid Mech. 530, 327–352. doi:https://doi.org/10.1017/S0022112005003824.

Leonardi, S., Orlandi, P., Smalley, R.J., Djenidi, L., Antonia, R.A., 2003. Direct numerical simulations of turbulent channel flow with transverse square bars on one wall. J. Fluid Mech. 491, 229–238. doi:10.1017/S0022112003005500.

McSherry, R., Chua, K., Stoesser, T., 2017. Large eddy simulation of free-surface flows. Journal of Hydrodynamics, Ser. B 29(1), 1–12. doi:https://doi.org/10.1016/S1001-6058(16)60712-6.

McSherry, R., Chua, K., Stoesser, T., Mulahasan, S., 2018. Free surface flow over square bars at intermediate relative submergence. Journal of Hydrodynamics, Ser. B 56(6), 825–843. doi:https://doi.org/10.1080/00221686.2017.1413601.

Nicoud, F., Ducros, F., 1999. Subgrid-scale stress modelling based on the square of the velocity gradient tensor. Flow Turbul. Combust. 62(3), 183–200. doi:doi:10.1023/A:1009995426001.

Okamoto, S., Seo, S., Nakaso, K., Kawai, I., 1993. Turbulent shear flow and heat transfer over the repeated two-dimensional square ribs on ground plane. J. Fluids Eng. 115, 621–637. doi:https://doi.org/10.1115/1.2910191.

Ouro, P., Fraga, B., Lopez-Novoa, U., Stoesser, T., 2018. Scalability of an eulerian-lagrangian large-eddy simulation solver with hybrid mpi/openmp parallelisation. Comput. Fluids. 179, 123–136. doi:https://doi.org/10.1016/j.compfluid.2018.10.013.

Ouro, P., Harrold, M., Stoesser, T., Bromley, P., 2017a. Hydrodynamic loadings on a horizontal axis tidal turbine prototype. J. Fluid Struct. 71, 78–95. doi:10.1016/j.jfluidstructs.2017.03.009.

Ouro, P., Stoesser, T., 2017b. An immersed boundary-based large-eddy simulation approach to predict the performance of vertical axis tidal turbines. Comput. Fluids. 152, 74–87. doi:10.1016/j.compfluid.2017.04.003.

Perry, A.E., Schofield, W.H., Joubert, P.N., 1969. Rough wall turbulent boundary layers. J. Fluid Mech. 32(2), 383–413. doi:10.1017/S0022112069000619.

Rodi, W., Constantinescu, G., Stoesser, T., 2013. Large-Eddy simulation in hydraulics. CRC Press. London .

Roussinova, V., Balachandar, R., 1969. Open channel flow past a train of rib roughness. J. Turbul. 12(28), 1–17. doi:https://doi.org/10.1080/14685248.2011.591399.

Sethian, J.A., Smereka, P., 2003. Level set methods for fluid interfaces. Annu. Rev. Fluid Mech. 35, 341–372. doi:10.1146/annurev.fluid.35.101101.161105.

Shu, C.W., 2009. High order weighted essentially nonoscillatory schemes for convection dominated problems. Siam Rev. 51(1), 82–126. doi:https://doi.org/10.1137/070679065.

Simpson, R.L., 1973. A generalized correlation of roughness density effects on the turbulent boundary layer. AIAA J. 11, 24–244. doi:https://doi.org/10.2514/3.6736.

Stoesser, T., 2010. Physically realistic roughness closure scheme to simulate turbulent channel flow over rough beds within the framework of les. J. Hydraul. Eng. 136(10), 812–819. doi:https://doi.org/10.1061/(ASCE)HY.1943-7900.0000236.

Stoesser, T., 2014. Large-eddy simulation in hydraulics: Quo vadis? Journal of Hydraulic Research 52(4), 441–452. doi:https://doi.org/10.1080/00221686.2014.944227.

Stoesser, T., McSherry, R., Fraga, B., 2015. Secondary currents and turbulence over a non-uniformly roughened open-channel bed. Water 7(9), 4896–4913. doi:10.3390/w7094896.

Stoesser, T., Nikora, V., 2008. Flow structure over square bars at intermediate submergence: Large eddy simulation study of bar. Acta Geophys. 56(3), 876–893. doi:https://doi.org/10.2478/s11600-008-0030-1.

Stoesser, T., Rodi, W., 2004. Les of bar and rod roughened channel flow. in: The 6th International Conference on Hydroscience and Engineering (ICHE-2004) .

Sussman, M., Smereka, P., Osher, S., 1994. A level set approach for computing solutions to incompressible two-phase flow. J. Comput. Phys. 114(1), 146–259. doi:https://doi.org/10.1006/jcph.1994.1155.

Tani, J., 1987. Turbulent boundary layer development over rough surfaces. Perspectives in turbulence studies. Springer. Berlin. .

		$\lambda/k = 5.2$, $H/k = 2.5$					
Case	U_b	U_τ	Re	Fr	Δx^+	Δy^+	Δz^+
Turbulent	0.24	0.073	7.2×10^3	0.44	58.3	68.3	36.4
Turbulent$_{\text{fine}}$	0.25	0.073	7.5×10^3	0.46	29.5	34.8	18.1
Turbulent$_{\text{double domain}}$	0.25	0.073	7.5×10^3	0.46	59.3	68.7	36.0
Transitional	0.23	0.073	6.9×10^2	0.42	5.8	6.8	3.6
Laminar	0.24	0.081	7.2×10^1	0.44	1.0	1.5	0.8
McSherry et al. (2018)	0.28	0.077	8.3×10^3	0.51	75.1	71.8	38.8
		$\lambda/k = 10.4$, $H/k = 2.9$					
Case	U_b	U_τ	Re	Fr	Δx^+	Δy^+	Δz^+
Turbulent	0.23	0.074	8.0×10^3	0.39	59.5	69.7	37.2
Turbulent$_{\text{fine}}$	0.24	0.075	8.3×10^3	0.41	30.2	35.4	18.9
Turbulent$_{\text{double domain}}$	0.24	0.075	8.3×10^3	0.41	60.4	70.7	37.7
Transitional	0.22	0.075	7.7×10^2	0.38	5.9	7.0	3.7
Laminar	0.23	0.11	8.0×10^1	0.39	1.3	2.0	1.1
McSherry et al. (2018)	0.24	0.083	8.3×10^3	0.42	80.3	76.9	41.0

Table 1: Hydraulic conditions and computational details.

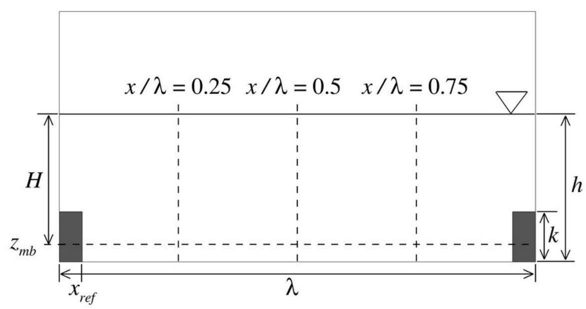

Figure 1: Schematic of the computational domain.

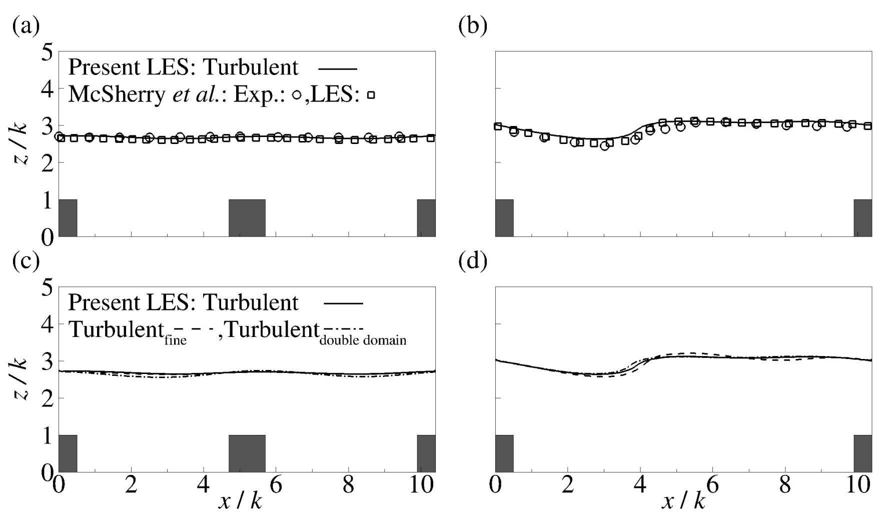

Figure 2: Time- and spanwise-averaged free surface elevations for (a,c) $\lambda/k = 5.2$ and (b,d) $\lambda/k = 10.4$.

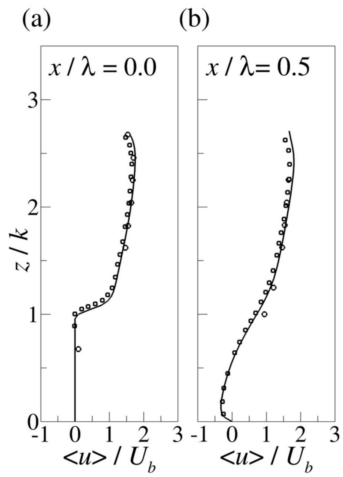

Figure 3: Temporal and spanwise mean streamwise velocity for $\lambda/k = 5.2$ at selected steamwise locations.

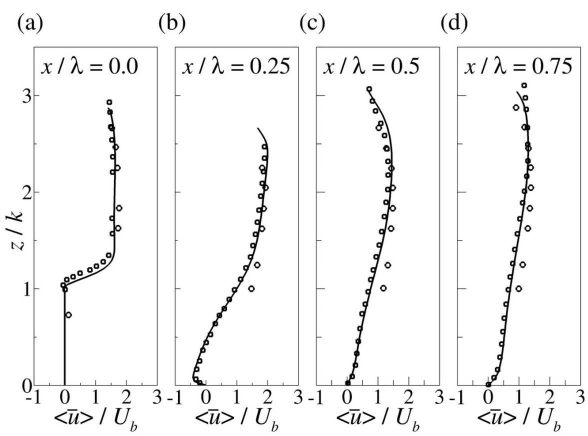

Figure 4: Time- and spanwise-averaged streamwise velocity for $\lambda/k = 10.4$ at selected steamwise locations.

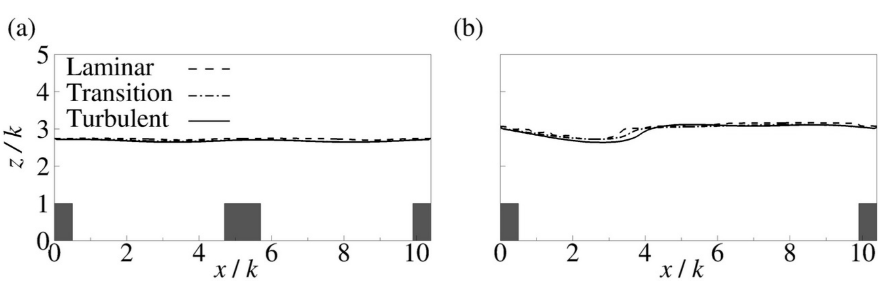

Figure 5: Time- and spanwise-averaged water surface profiles in turbulent, transitional and laminar flow for (a) $\lambda/k = 5.2$ and (b) $\lambda/k = 10.4$.

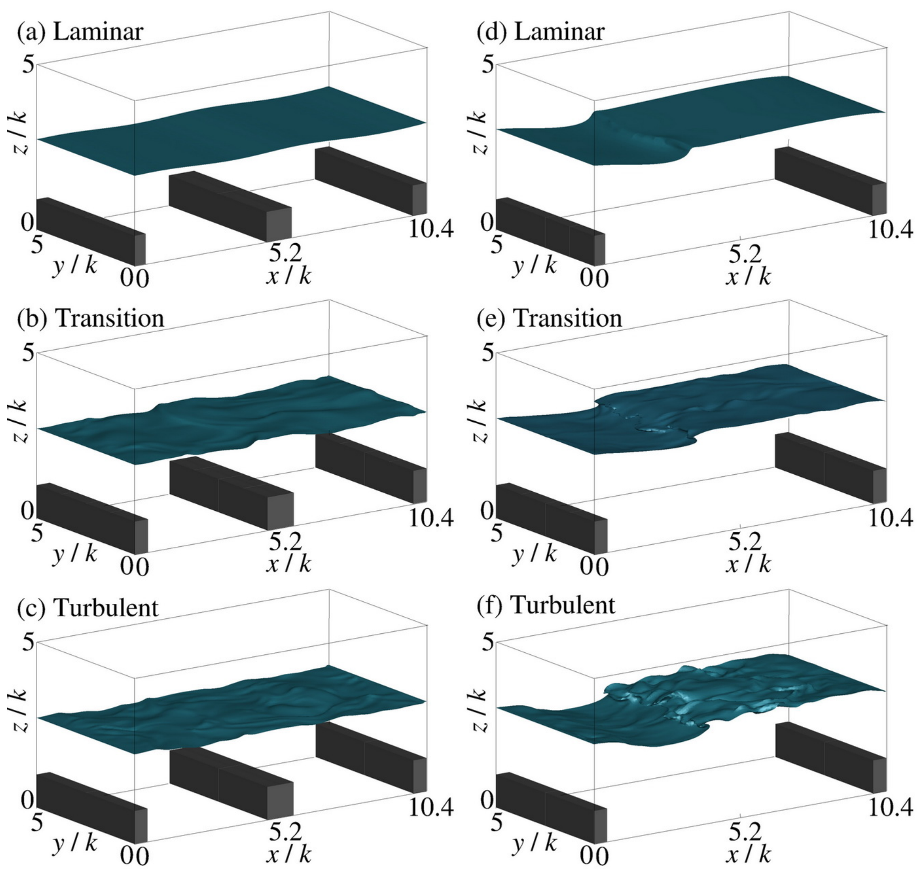

Figure 6: Instantaneous water surface in turbulent, transitional and laminar flow for (a-c) $\lambda/k = 5.2$ and (d-f)$\lambda/k = 10.4$.

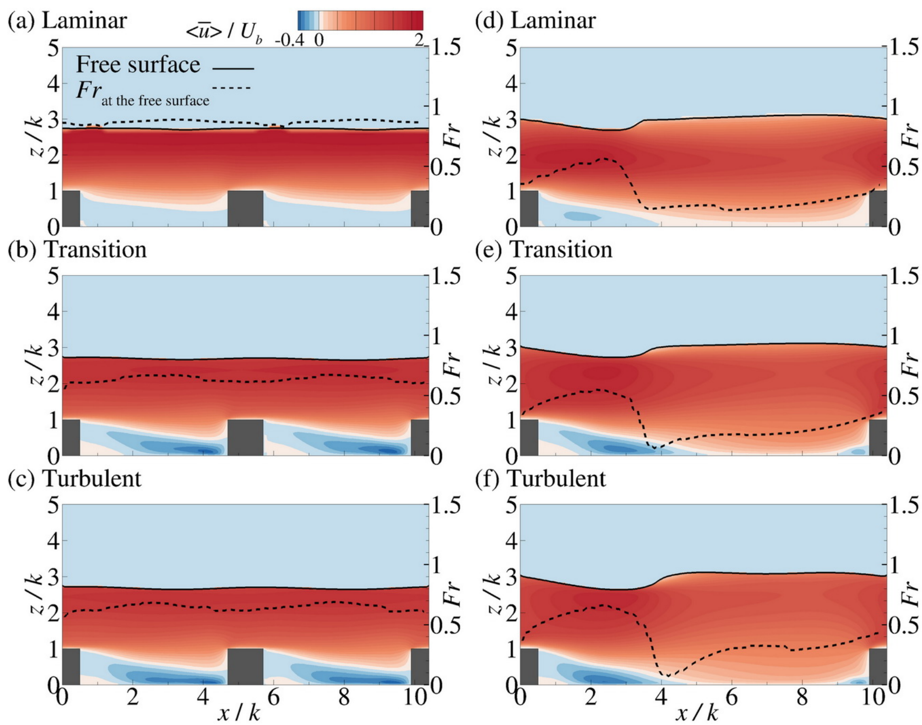

Figure 7: Contours of the time- and spanwise-averaged streamwise velocity together with the local Froude number at the water surface for turbulent, transitional and laminar flow for (a-c) $\lambda/k = 5.2$ and (d-f) $\lambda/k = 10.4$.

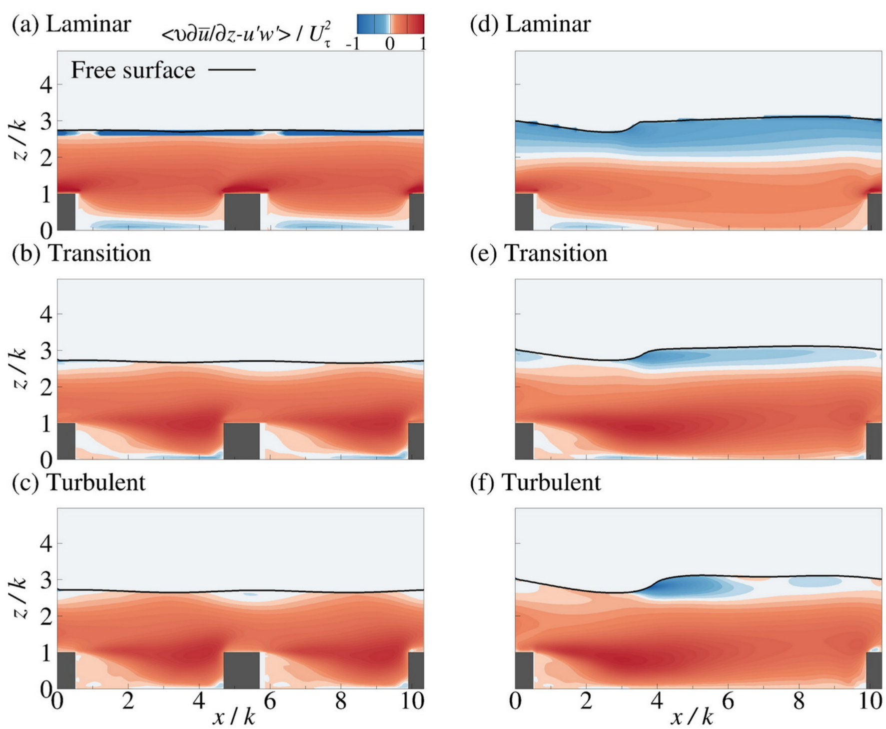

Figure 8: Contours of time- and spanwise-averaged viscous and Reynolds shear stresses in turbulent, transitional and laminar flow for (a-c) $\lambda/k = 5.2$ and (d-f) $\lambda/k = 10.4$.

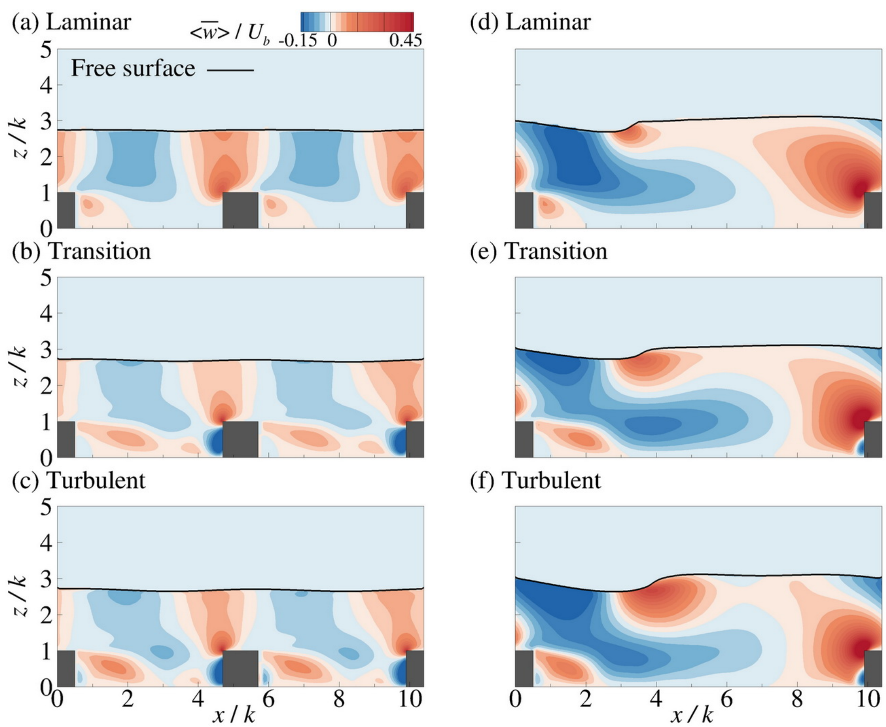

Figure 9: Time- and spanwise-averaged wall-normal velocity in turbulent, transitional and laminar flow for (a-c) $\lambda/k = 5.2$ and (d-f) $\lambda/k = 10.4$.

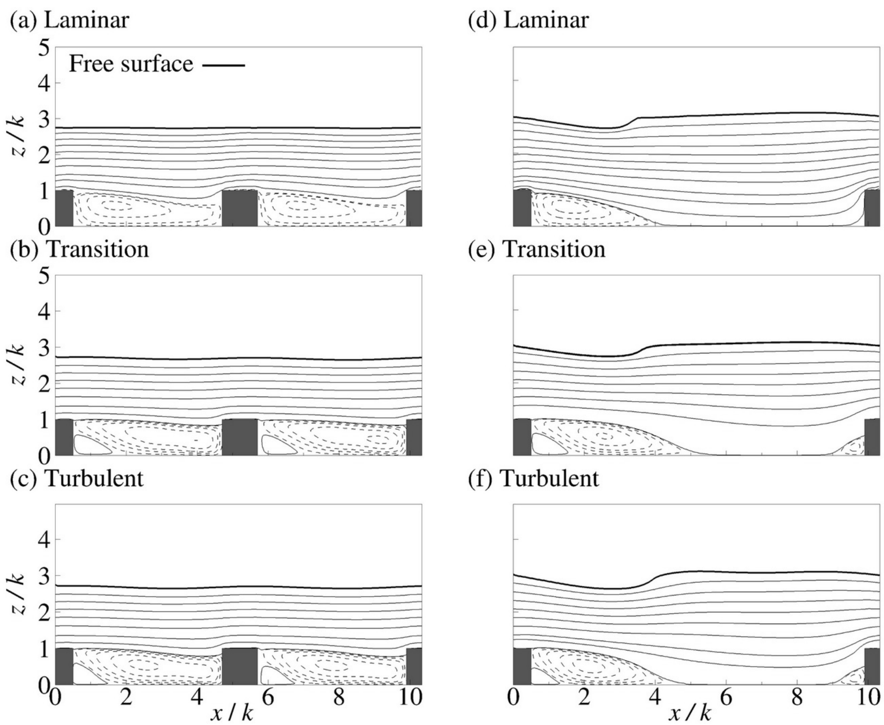

Figure 10: Contour lines of the spanwise-averaged streamfunction in turbulent, transitional and laminar flow for (a-c) $\lambda/k = 5.2$ and (d-f) $\lambda/k = 10.4$.

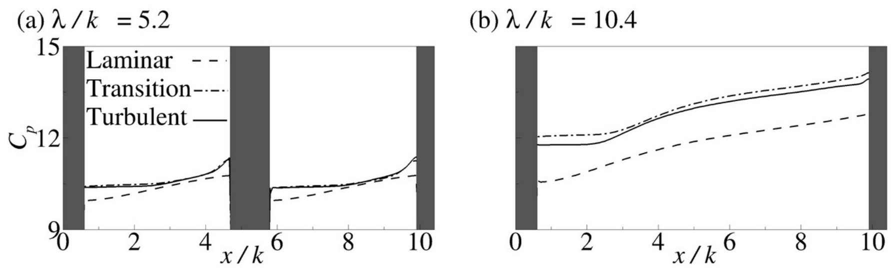

Figure 11: Pressure coefficient in turbulent, transitional and laminar flow for (a) $\lambda/k = 5.2$ and (b) $\lambda/k = 10.4$.

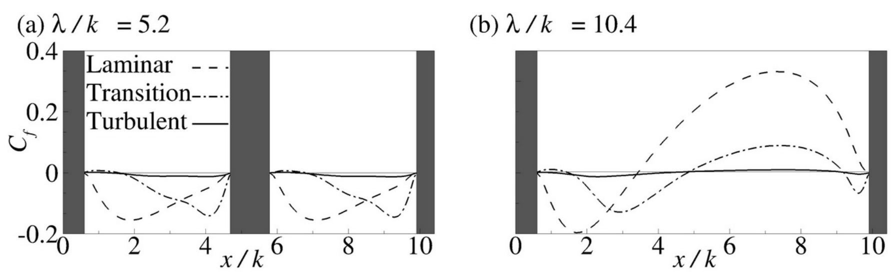

Figure 12: Friction coefficient in turbulent, transitional and laminar flow for (a) $\lambda/k = 5.2$ and (b) $\lambda/k = 10.4$.

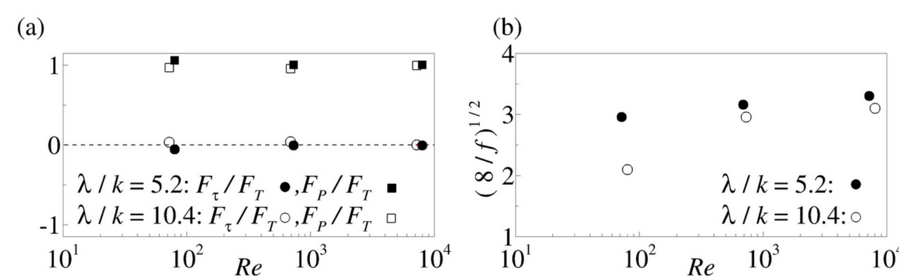

Figure 13: (a) Friction and pressure forces, (b) variation of friction factor with Reynolds number.